J Mater Sci (2007) 42:2236–2243
DOI 10.1007/s10853-006-0536-3

Production and characterization of pure and Cr^{3+}-doped hydroxyapatite for biomedical applications as fluorescent probes

Tatiana S. de Araujo · Zélia S. Macedo · Petrus A. S. C. de Oliveira · Mário E. G. Valerio

Received: 8 November 2005 / Accepted: 6 June 2006 / Published online: 27 February 2007

Abstract Pure and Cr^{3+}-doped hydroxyapatite (HAP) were prepared via chemical precipitation route. The XRD measurements revealed that the typical HAP powder pattern was obtained. SEM analysis indicated that aggregates of nanoparticles were formed. EDX analysis indicates that the [Ca]/[P] concentration ratio was higher than the expected values but can be explained by the presence of carbonate groups as dopants. The optical absorption spectra of the doped samples presented absorption bands typical of Cr^{3+} occupying to different crystalline sites. From the position of the bands, it was possible to estimate the crystal field parameters for both sites of Cr^{3+} in the HAP matrix. The emission spectra of the Cr-doped samples were also investigated and typical transitions of the dopant ion, in trivalent state, were identified. The potential use of the Cr^{3+}-HAP as fluorescent probes for medical applications was discussed.

Introduction

Hydroxyapatite (HAP) is the primary natural and inorganic component of the bones and teeth. Artificial HAP is highly biocompatible and can be easily incorporated in biological tissues [1]. In bone implants, HAP stimulates bone growth and no undesirable side effects were observed [2, 3]. Small HAP particles were also found to be biodegradable [2, 3].

Many different methods can be found in the literature to produce HAP either using chemical or physical routes. The main chemical routes are precipitation, hydrolysis, and sol–gel methods and the main physical route is the solid state synthesis. Physical routes have the advantages of relative simplicity and good reproducibility. On the other hand, the chemical routes normally produce homogeneous and reactive biomaterial with better control of the stoichiometric composition [4, 5].

Hydrothermal methods produces nanocrystalline HAP powders with uniform shapes and particle sizes, while sol–gel routes normally forms irregular shape powders [1]. HAP produced via precipitation routes in aqueous solutions showed similar sizes and shapes to the HAP found in bones and teeth. Rodríguez et al. [6] studied the HAP precipitated from the reaction of solutions of $Ca(NO_3)_2{\cdot}4H_2O$ and $(NH_4)_2HPO_4$, with a solution of NH_4OH to control the pH. The pH is a key experimental parameter to produces HAP via precipitation routes. Due to the recrystallization of $(NH_4)_2HPO_4$, it was impossible to conduct experiments at pH > 10. On the other hand, experiments developed at an initial pH 7 or 8 resulted in final pH lower than 4. As a consequence, the obtained powder was not identified as apatite but as dicalcium phosphate, either brushite, monetite, or a mixture of both phases, depending on other parameters such as temperature [6].

T. S. de Araujo · Z. S. Macedo · M. E. G. Valerio (✉)
Departamento de Física-DFI, Universidade Federal de Sergipe, Campus Universitário, Sao Cristovao CEP 49100-000, SE, Brasil
e-mail: mvalerio@fisica.ufs.br

P. A. S. C. de Oliveira
Departamento de Química Fundamental-DQF, Universidade Federal de Pernambuco, Av Prof. Luiz Freire s/n, Recife CEP 50670-901, PE, Brasil

Crystal sizes of HAP samples precipitated at 25 °C are in the range of human bone or dentin while crystal sizes of the sample obtained at 90 °C are in the range of dental enamel. Longer reaction times yield apatites with higher Ca/P ratios, resulting in a decrease of the calcium deficiency of the sample. When the reactions are carried out at 90, 2 h are enough to obtain a product with a Ca/P ratio of 1.67 [6].

The above results found in the literature indicates that the stoichiometry, the degree of crystallinity and the morphology of HAP are very sensitive to the preparation conditions and, in order to attain good reproducibility, very careful experimental procedures have to be adopted. In all chemical precipitation routes, the important experimental parameters that have to be controlled are: pH, temperature, concentration of the reagents, Ca/P ratio in the starting solutions and storage time [6–8].

Wakamura et al. [8] studied the structure, morphology and thermal stability of Cr^{3+}-doped HAP obtained via chemical routes. The Ca/P ratios grows from 1.66 to 3.25 with the increase of the molar fraction of Cr^{3+} and the authors explained this result as due to the formation of a new crystalline phase.

In the present work a methodology to produce HAP was evaluated and adapted to produce micro and nano-sized particles. Cr^{3+} was incorporated as dopant in the material aiming the development of a biosensor based on the fluorescent properties of the Cr^{3+} ion. Any biocompatible material marked with a fluorescence probe, in principle, can be followed in the human body via the typical fluorescence signal of the marker if the luminescence wavelengths (emission and/or excitation) of the marker are different from the strong fluorescence signal of some of the body fluids. The aim of the present work was to test if the Cr^{3+} in HAP can satisfy such condition. The dopant was choosen due to its low toxicity and known absorption, emission and excitation spectra. The low toxicity of Cr^{3+} is partially due to the fact that many Cr(III) complexes are poorly soluble at physiological pH values and are not easily transported through the cell membranes. Complexes which are not able to penetrate into the cells may not induce toxic responses [9, 10].

Concerning the spectroscopic properties, the ground state of Cr^{3+} in a octahedral coordination environment is always $^4A_{2g}$. The excited states, however, depend strongly on the interactions with the crystalline matrix. In an octahedral environment the energy levels of Cr^{3+} can be rationalized using the crystal-field (Dq) and Racah (B) parameters [11–13]. Many Cr^{3+}-doped systems can be found in the literature due to the known lasing action of Cr-based solid-state matrix, like ruby [11, 13] and $LiSrAlF_3$ [14, 15]. Very few phosphate based materials were doped with Cr^{3+}. Ravikumar et al. [16] have studied the optical properties of the Cr^{3+} in $ZnNH_4PO_4{\cdot}6H_2O$ and they were able to identify the main optical transitions associated to the Cr^{3+} doping ion. To our knowledge, there is no study in the literature concerning the identification of the Cr^{3+} transitions in doped-HAP and this information is crucial if the Cr^{3+}-doped HAP is intended to be used as fluorescent biosensor. In the present work, the characterization of the Cr^{3+} optical transitions inside the HAP matrix are also done via absorption, emission and excitation spectroscopy and the potential use of such transitions are discussed.

Experimental setup

The samples of hydroxyapatite (HAP) were produced using a precipitation route based on the following reaction [6]:

$$10Ca(NO_3)_2 \cdot 4H_2O + 6(NH_4)_2HPO_4 + 8NH_4OH \rightarrow Ca_{10}(PO_4)_6(OH)_2 \downarrow + 20NH_4NO_3 + 6H_2O \quad (1)$$

A 0.167 M solution of $Ca(NO_3)_2{\cdot}4H_2O$ was slowly added to a 0.1 M $(NH_4)_2HPO_4$ solution at a rate of 1.5 mL/min under continuous agitation. The pH was adjusted during the mixing using a solution of NH_4OH. The final mixture was then kept at room temperature for different maturation time intervals from 50 h to 150 h. The obtained solutions were filtered, rinsed and then dried and calcined at 500 °C during 1 h. For the Cr^{3+}-doped samples, a 0.01 M solution of $Cr(NO_3)_3{\cdot}9H_2O$ was added to the Ca solution, giving a Cr/Ca concentration ratio of 0.06.

The precipitated HAP powders were characterized using powder X-ray diffraction (XRD), Scanning Electron Microscopy (SEM) and Energy Dispersive X-Ray fluorescence (EDX) techniques. The optical absorption and the emission and excitation fluorescence spectra of the doped samples were also investigated.

Powder XRD measurements were performed at room temperature in a Rigaku DMAX2000 diffractometer using CuKα radiation at 40 kV/40 mA equipped with a monochromator. The powder samples were dispersed in glass plates and inserted in the rotary sample holder.

SEM images were obtained in a JEOL JSM-5900EDX microscope and the EDX analyses were done inside the microscope using a Noran Instruments 695A-1SPS system. The images were taken in different

instrumental magnification from ×50 up to ×100,000 with resolutions down to the nanometer scale for the highest magnification.

Optical absorption spectra were recorded in a Perkin-Elmer spectrophotometer from 200 nm to 1,000 nm, with a 1 nm resolution, at room temperature. The pure and doped HAP nanoparticles were suspended in deionized water in 1 cm optical path quartz cuvettes. OA spectra of the cuvettes and the deionized water were measured separately to assure that none of the cuvette or the water absorption bands were superposed to the ones of the HAP samples.

The luminescence measurements were carried out at room temperature in a ISS/PC1 spectrofluorimeter equipped with a 300 W Xe lamp. The excitation and emission wavelength bandwidth were 8 and 4 nm, respectively. The samples were pressed and conformed as pellets of 6 mm of diameter and 1 mm thickness.

Results and discussions

The pure and doped HAP samples were produced in constant pH of 10.4. Lorenzo and Regi [6] found that when the reaction (1) was carried out at pH > 10, HAP is mainly formed and other phosphates, like $(NH_4)_2HPO_4$ or $CaHPO_4$, seemed to be unstable. Wakamura et al. [8] studied the crystallization of Cr^{3+}-doped HAP using a different precipitation route in pH 9. They found that for different concentrations of Cr^{3+} up to [Cr]/[Ca] = 0.5, only the HAP diffraction pattern was observed. In our case, the pH 10,4 was chosen to prevent that other phosphates, apart from HAP, are formed during the reaction.

Figure 1 shows the XRD patterns of pure (a) and 6 mol% Cr^{3+}-doped (b) HAP samples for three different maturation times, 50, 100 and 150 h. The standard HAP XRD pattern (PDF (84-1998) is also shown in the bottom part of the figures. In all cases, the XRD results show that only the HAP crystalline phase was obtained and this result is consistent with the Lorenzo and Regi [6] results. In the doped sample, no change in the lattice parameters of HAP was observed. This is due to the low concentration of Cr^{3+} in the samples. Also, 6 mol% of the dopant was not enough to form another crystalline phase apart from the HAP one indicating that the dopant ion was successfully dissolved in the HAP matrix. This latter result is consistent with the XRD powder diffraction study of Wakamura et al. [8].

There are no substantial differences in the XRD patterns as a function of the maturation time indicating that this experimental parameter is not important from the crystallographic point of view. The same result was also observed for the doped samples.

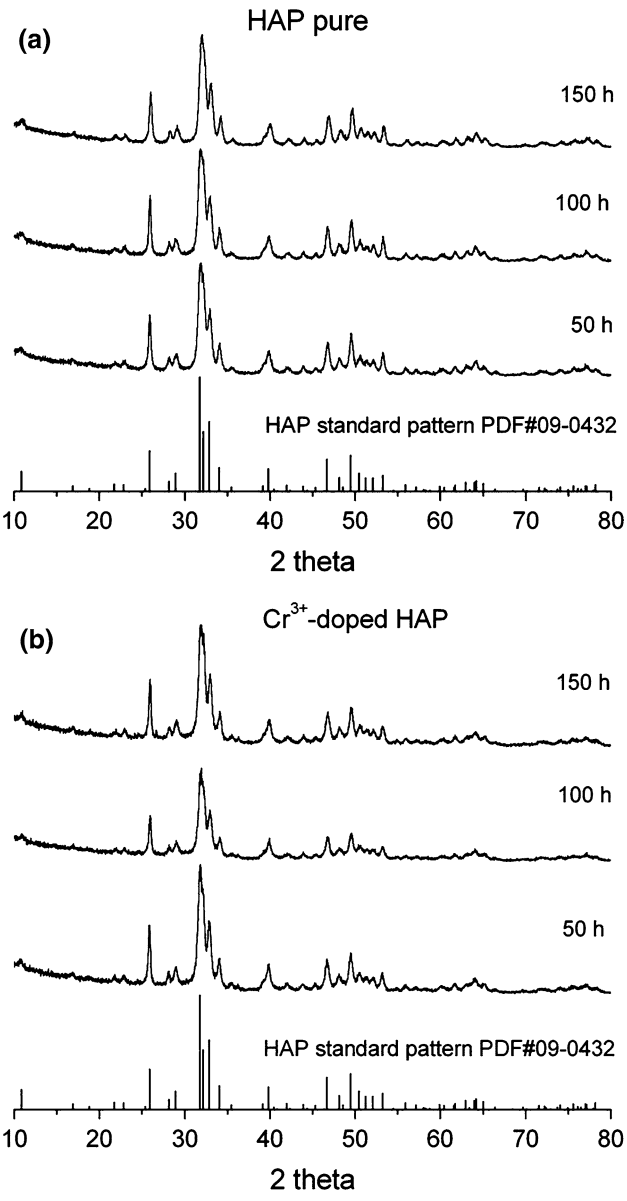

Fig. 1 XRD powder patterns of hydroxyapatite producted at different maturation time, as compared to the HAP standard pattern PDF 84-1998 (shown in the bottom part of the figures): (**a**) pure samples (**b**) Cr^{3+}-doped samples

The relatively broadening of the XRD peaks indicates that the sizes of the crystallite grains are rather small. Using the Scherrer formula within the JADE Rigaku computer code and the [002], [310], [222] and [004] diffraction peaks, the crystallite sizes were estimated. The results are shown in Table 1 for the pure and doped samples. The sizes are found to independent of the maturation time and also independent of the dopant, within the experimental errors. The average crystallite size is about 26 nm.

Table 1 Crystallite sizes of the pure and doped HAP samples prepared using different maturation time at room temperature

$Ca_{10}(PO_4)_6(OH)_2$			
Maturation time (h)	50	100	150
Crystallite size (nm)	25 ± 1	27 ± 1	23 ± 1
$Ca_{9.94}Cr_{0.06}(PO_4)_6(OH)_2$			
Maturation time (h)	50	100	150
Crystallite size (nm)	26 ± 1	28 ± 1	26 ± 1

Figure 2 shows typical SEM images of the pure HAP powders obtained with different instrumental magnification. Figure 2a shows that the powder samples are mainly formed by agglomerates with different shapes and sizes in the micrometer range. As the magnification increases, the detailed structure of such agglomerates was revealed. Figure 2d, obtained with a ×100,000 magnification, showed that the agglomerates are formed by spherical shape particles in the nanometer range. The same analysis were done for the Cr^{3+}-doped samples and it was observed that these samples were also formed by agglomerates of nanoparticles but the shape of such nanoparticles is now ellipsoidal, as shown in Fig. 3.

Form the SEM micrographs it is possible to calculate the grain sizes and it was found that for both the pure and doped samples the nanoparticles are about 40–100 nm sizes. It is also noted that the particle sizes of the samples are similar to the HAP found in human bones and dentin. Comparing the average particle sizes obtained via the SEM micrographs with the crystallite sizes obtained via the Scherer method, it is possible to conclude that each nanoparticle is actually composed by 2–4 crystallites.

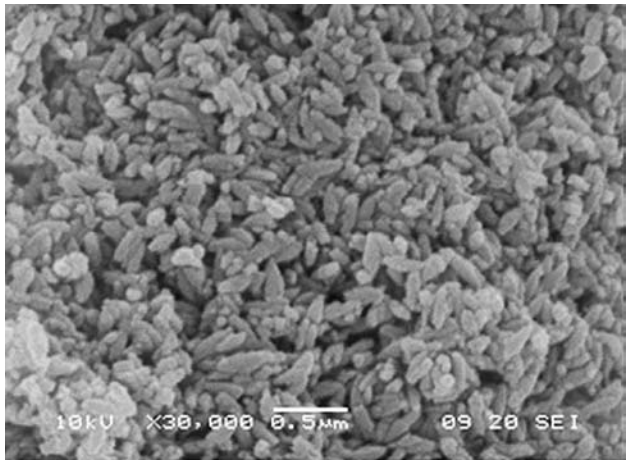

Fig. 3 SEM micrographs of the 6 mol% Cr^{3+}-doped HAP powders prepared with a maturation time of 100 h. The micrograph was obtained using a ×30,000 instrumental magnification

The concentrations of Ca, P and Cr in the samples were done via EDX. The results in terms of the molar concentration ratios are shown in Table 2 for samples prepared using different maturation times. The expected [C]/[P] ratio is 1.67, according to the stoichiometry of pure HAP. Considering the experimental error bars, the results presented in Table 2 indicates that the [Ca]/[P] ratio of the pure HAP powder is independent on the maturation time. In all pure samples this ratio is higher than the expected one and they are around 1.94. It means that the samples are about 16% P deficient, but these values are within the [Ca]/[P] limits that the HAP structure can accommodated [18]. They

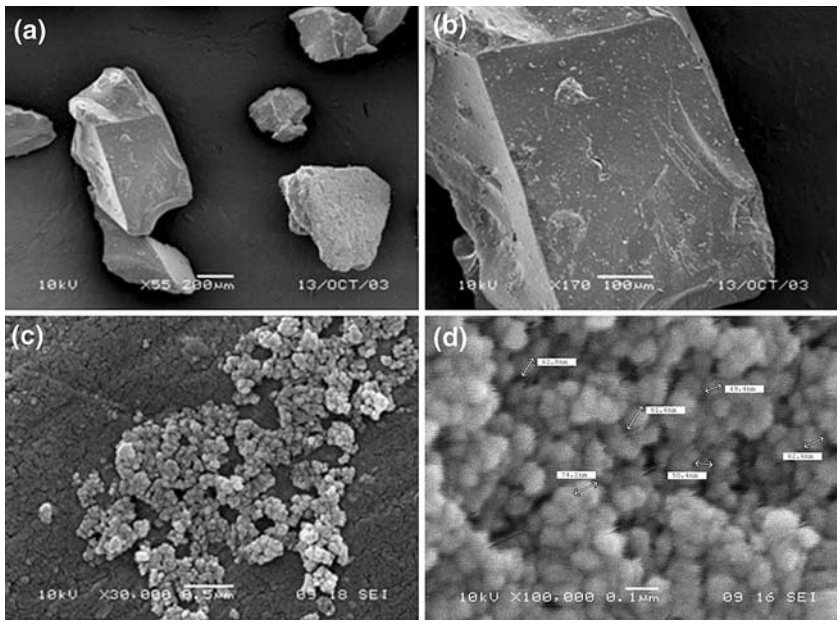

Fig. 2 SEM micrographs of the pure HAP powders prepared with a maturation time of 100 h. Instrumental magnification: (**a**) ×55, (**b**) ×170, (**c**) ×30,000, (**d**) ×100,000

Table 2 Cation molar concentration ratios obtained via EDX measurements of the pure HAP and Cr^{3+}-doped samples prepared using different maturation time

Maturation time (h)	Theoretical [Ca]/[P]	Experimental [Ca]/[P]		
$Ca_{10}(PO_4)_6(OH)_2$				
50	1.67	1.93 ± 0.02		
100		1.95 ± 0.02		
150		1.93 ± 0.02		
$Ca_{10-x}Cr_x(PO_4)_6(OH)_2$ Maturation time (h)	Theoretical $\frac{[Ca]+[Cr]}{[P]}$	Experimental $\frac{[Ca]+[Cr]}{[P]}$	Expected $\frac{[Cr]}{[Ca]}$	Experimental $\frac{[Cr]}{[Ca]}$
50	1.67	2.02 ± 0.12	0.06	0.056 ± 0.003
100		2.04 ± 0.10		0.068 ± 0.002
150		2.00 ± 0.26		0.050 ± 0.006

are also compatible to the values found in the mineral part of human bones that ranges from 1.61 up to 1.87 [17].

Synthetic HAP, that are similar to the HAP of human bones and tooth, contains carbonate groups, as shown by Miyake et al. [18]. The carbonate groups occupy phosphate sites leading to P deficiency. Miyake et al. obtained a concentration ratio of 1:10 phosphate to carbonate substitution in their samples. The pure HAP samples in the present work were prepared in air and thus there is a reasonable chance that carbonates are formed via reaction of the hydroxyl groups in the aqueous solution with the CO_2 present in the atmosphere forming H_2CO_3 that is easily dissolved in water. The carbonate groups are then free to be incorporated in the HAP nanoparticles occupying the phosphate sites in the HAP structure. This substitution, however, did not cause appreciable change in the XRD pattern of HAP since the X-Ray scattering factors for phosphates and carbonates are not very different and the amount of phosphate substitution by carbonates is quite low, around 16% according to the EDX results, below the detection limit of XRD in this particular case. On the other hand, the reabsorption of implants made with HAP is faster when carbonate groups are present in the HAP structure [10]. This is another advantage of the methodology adopted in the present work, an easy incorporation of carbonate groups in the nanoparticles.

In the case of the Cr^{3+}-doped samples, the values in Table 2 indicates that the stoichiometry deviation of the ([Ca] + [Cr])/[P] ratios are higher than the [Ca]/[P] ratios for the pure samples. Again it is possible to see that, within the experimental errors, the ([Ca] + [Cr])/[P] ratios did not dependent upon the maturation time. The average value is 2.02 indicating now that the P deficiency in these samples is about 21% as compared to the stoichiometric HAP. In the doped samples, apart from the incorporation of carbonate groups, other mechanism can cause deviation from stoichiometry. Ishikawa et al. [19] found that incorporation of other cations can give [Ca]/[P] ratios ranging from 1.61 up to 2.00, and this seems to be case in the Cr^{3+}-doped samples of the present work.

The [Cr]/[Ca] molar concentration ratios were also evaluated for the doped samples, also shown in Table 2. Within the experimental errors of the EDX method, the experimental values are reasonable close to 6 mol%, the starting concentration ratio of the doped samples.

Optical absorption (OA) measurements were done in the pure and doped HAP nanopowders suspended in deionized water. In Fig. 4 the optical absorption of the pure HAP was shown in the top part of the figure. In the bottom, the optical absorption of the Cr^{3+}-doped sample was recorded using the pure HAP as reference.

The OA curves of the pure HAP sample can be used to estimate the optical band gap of the material. Generally the equation (written here in a simplified

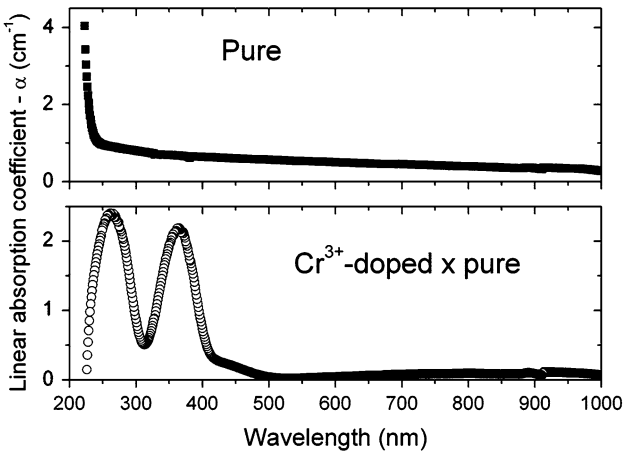

Fig. 4 Optical absorption of the pure sample (top) measured using air as reference. The bottom plot shows the OA of the Cr^{3+}-doped sample measured using the pure sample as the reference

form) used to determine the band gap nature and the value of E_g, the gap energy is [19, 20]:

$$\alpha = \frac{c}{h\nu}(h\nu - E_g)^n \quad (2)$$

where c is a constant nearly independent on photon energy $h\nu$ and known as the disorder parameter. The value of the optical energy gap E_g is obtained by plotting $(\alpha h\nu)^{1/n}$ in the high absorption range followed by extrapolating the linear region of the plot $(\alpha h\nu)^{1/n} = 0$. This extrapolated value is used to define the so-called optical gap. The plots of $(\alpha h\nu)^{1/n}$ against hν was tested for different values of n = 1/2, 3/2, 2 and 3 and the best linear relation was obtained for n = 2. This indicates that allowed direct transitions are responsible for absorption in HAP [20]. In Fig. 5a, the experimental and the fitted curves are shown. The optical energy gap determined for HAP is (5.05 ± 0.30) eV.

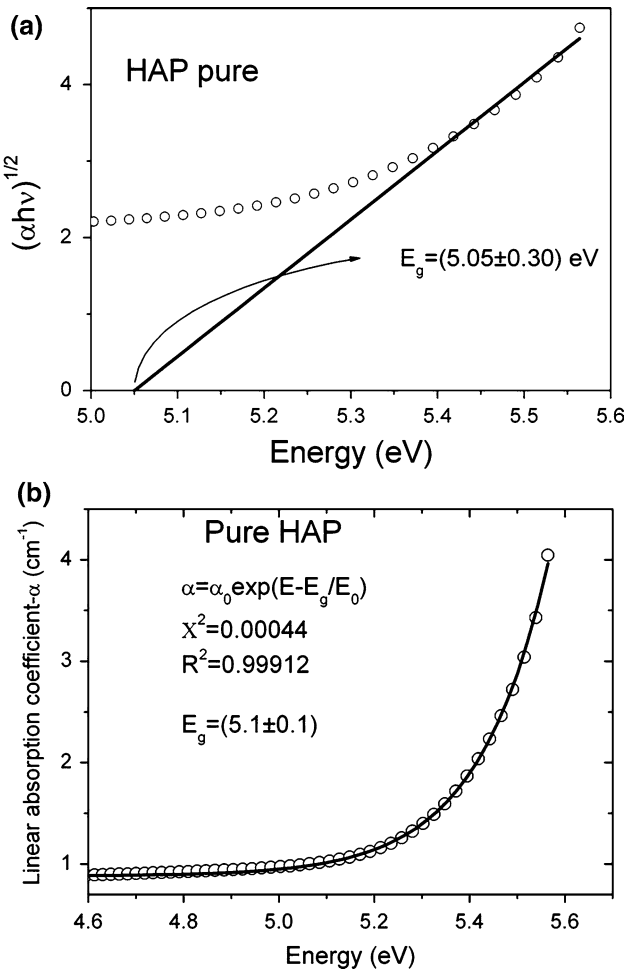

Fig. 5 Models used to estimate the optical gap of hap. (**a**) Eq. 2. (**b**) Urbach rule. Value sof E_g are also shown in the figures

Another approach is to considerer the spectral region close to the absorption border follows the Urbach rule [21, 22] given by

$$\alpha(E) \propto e^{\frac{\sigma(E-E_{gap})}{k_B T}} \quad (3)$$

where σ is a fitting parameter, E is the photon energy, k_B is Boltzmann's constant and T is the temperature. The experimental absorption curves for the pure HAP samples were fitted to this expression given the energy gap value E_{gap}, as shown in Fig. 5b. The Urbach rule describes quite well the absorption of the HAP samples close to the edge and the obtained value of E_{gap} was (5.1 ± 0.1) eV.

Both methods, via Eq. 2 and via Urbach rule, gave compatible values of about 5.1 eV for the energy gap of HAP. This value is also very close to the value of 5 eV estimated by Calderín et al. [23] via ab initio calculations.

The OA of the doped samples were converted to the energy (or wave number) scale, as shown in Fig. 6, in order to obtain the crystal field Dq and Racah parameters, B and C. It was observed that each one of the three absorption peaks is actually composed by two peaks. Best fit of Gaussian type peaks gave the continuous line drawn in Fig. 6 and the individual peaks are displayed as broken lines. The fitting is very good with a χ^2_{red} = 0.0002 and a correlation factor of 0.99976. The interpretation of such result is as follows: there are two no-equivalent Ca sites in the HAP structure (CaI and CaII) and the Cr^{3+} dopant can

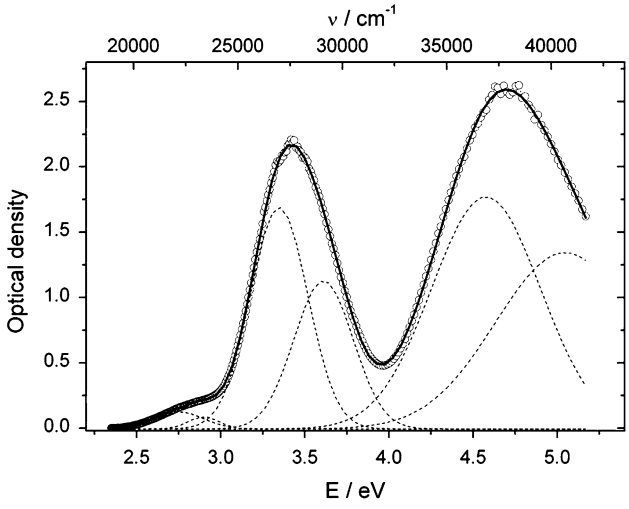

Fig. 6 Optical density of the doped sample plotted as function of the photon energy (bottom axis) and wave numbers (upper axis). Continuous line indicates the best fit model considering six Gaussian peaks and the broken lines represents the individual absorption peaks

substitute at either one of these sites. Both Ca sites exhibit slightly distorted octahedral symmetry meaning that there are two non-equivalent Cr^{3+} ions (CrI and CrII) in the doped HAP samples. Based on this assumption, the crystal field, Dq, and Racah parameters, *B* and *C*, CrI and CrII could be evaluated using the appropriate Tanabe-Sugano diagram. The following values were obtained: Dq = 2,697 cm^{-1}, *B* = 974.3 cm^{-1}, for Cr type I and Dq = 2,910 cm^{-1}, *B* = 1,163 cm^{-1}, for Cr type II. C = 4.5*B* for both types. Using these values, it was possible to identify each of the transitions observed in the OA spectra of the doped samples and they were shown in Table 3. Also in Table 3 it was shown the experimental values of the OA bands as compared to the calculated values of each transition using the Dq, *B* and *C* parameters above and the energy level dependency of each level as described by Powel [24].

The agreement between the experimental and calculated wavelengths of the first two spin-allowed transitions is very good. The third transition $^4A_2(F) \rightarrow {}^4T_1(P)$ are not seem because the required photon energies (about 7.3 eV, for CrI, and 8 eV, for CrII) are above the band gap of HAP. The same reason also applies for all the spin-forbidden transitions ($^4A_2(F) \rightarrow {}^2A_1(G)$, $^2T_2(H)$, $^2E(H)$, $^2T_1(H)$, $^2T_2(D)$) with calculated wavelengths lower than 242 nm corresponding to 5.1 eV, the band gap of HAP. The spin-forbidden $^4A_2(F) \rightarrow {}^2T_2(G)$ transition, with calculated wavelengths of 322 nm, for CrI and 273 nm, for CrI, are not seem because they are weak transitions superposed to the main spin-allowed transitions.

The emission and excitation spectra of the Cr^{3+}-doped HAP samples were measured at room temperature. The main feature of the spectra in the visible range is a broad emission around 454–464 nm when the excitation changes from 280 nm to 310 nm. This emission, however, are not suitable for applications of Cr^{3+}-doped HAP as biosensors since most of the body fluids are known to exhibit strong emissions in this spectral region when excited with UV lights. Nevertheless, when the excitation is shifted to 243 nm, the doped HAP displays a strong broad emission peaking at 320 nm, as shown in Fig. 7. This emission is composed by two bands peaking at 319 and 345 nm associated to the $^4T_1(F) \rightarrow {}^4A_2(F)$ transitions of CrI and CrII, respectively. This broad emission is characteristic of the Cr^{3+} in HAP, since the pure sample did not show any emission in this range.

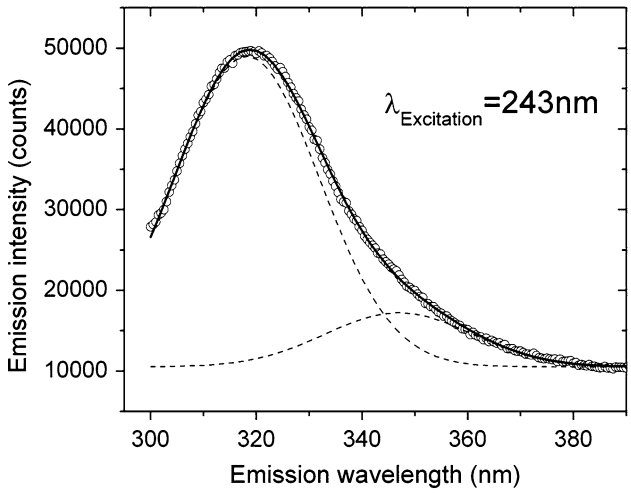

Fig. 7 Emission spectra of the Cr^{3+}-doped HAP sample. Excitation wavelength is 243 nm. Emission is associated to the $^4T_1(F) \rightarrow {}^4A_2(F)$ transitions of the Cr ions

Table 3 Experimental and calculated wavelengths λ of the Cr^{3+} transitions in HAP

All transitions are from the $^4A_{2g}(F)$ ground state to the excited states listed in the first column. Calculated values were obtained with the following crystal field and Racah parameters: Dq = 2,697 cm^{-1}, *B* = 974.3 cm^{-1}, for Cr type I and Dq = 2,910 cm^{-1}, *B* = 1,163 cm^{-1}, for Cr type II (see details in the text) *C* = 4.5*B* for both Cr types

Transitions: $^4A_2(F)$ to	Cr_I		Cr_{II}	
	λ_{Exp}	λ_{Calc}	λ_{Exp}	λ_{Calc}
Spin-allowed transitions				
$^4T_2(F)$	371	371	344	344
$^4T_1(F)$	271	271	246	246
$^4T_1(P)$	–	171	–	156
Spin-forbidden transitions				
$^2T_1(G)$	451	471	429	396
$^2E(G)$		490		413
$^2T_2(G)$	–	322	–	273
$^2A_1(G)$	–	227	–	202
$^2T_2(H)$	–	212	–	188
$^2E(H)$	–	200	–	177
$^2T_1(H)$	–	183	–	161
$^2T_2(D)$	–	162	–	142

Conclusions

Pure and Cr^{3+}-doped HAP powders were successfully prepared in the present work following a chemical precipitation route. The samples were analyzed via XRD powder diffraction and it was found that, for both pure and doped samples, only the HAP phase was produced. The crystallite sizes were evaluated via Scherrer formula giving an average value of 26 nm for all samples.

SEM images indicated that the samples are formed by micrometer-sized agglomerates of nanoparticles. The size of the nanoparticles were obtained directly from the SEM images and the values ranged from 40 nm to 100 nm. Combining these results with XRD ones, it is possible to conclude that each nanoparticle is composed by 2–4 crystallites.

EDX measurements inline with SEM indicated that the average [Ca]/[P] concentration ratios in the pure samples are around 1.94, 16% higher than the expected values of 1.67. This difference can be explained by incorporation of carbonate groups substituting the phosphate ones in the HAP matrix. This is an advantage of the chemical route used in the present work since the carbonate groups are known to accelerate the re-absorption of HAP implants [10]. In the Cr^{3+}-doped samples, the EDX results indicates a higher degree of deviation from stoichiometry, with ([Ca] + [Cr])/[P] ratios of about 2.02, 21% higher that the 1.67 expected value. This indicates that the dopant enhanced the incorporation of carbonate groups.

From the optical absorption spectra of the pure samples it was possible to obtain the optical energy gap of HAP. Two different approaches gave $E_g = 5.1$ eV, very close to the 5.0 eV value obtained by Calderín et al. [23] via ab initio calculations.

The typical OA spectra of Cr in the 3+ state (d^3 electronic configuration) were recorded for the doped samples. Two non-equivalents Cr^{3+} were found in HAP matrix corresponding to substitutions at both CaI and CaII crystallographic sites. All the main transitions of CrI and CrII were identified and the crystal field, Dq, and the Racah parameters, B and C, were evaluated.

Emission spectra of the Cr^{3+}-doped HAP excited at 243 nm reveals a strong fluorescent emission peaking at about 320 nm attributed to the $^4T_1(F) \rightarrow {}^4A_2(F)$ transitions of CrI and CrII. This emission is suitable for potential application as biosensors.

In conclusion, Cr^{3+} ion was successfully incorporated in the HAP matrix and this system can be used as a fluorescent probe for in vivo or in vitro applications due to the excellent biocompatibility of HAP combined to the low toxicity of the Cr^{3+} ion.

Acknowledgements The authors wish to thank the Brazilian funding agencies FINEP, CNPq and CAPES for financial support. This work was done within the CNPq/RENAMI and MCT/CNPq/PADCTIII programs. The authors are also thankful to Dr Francisco Rangel for helping with SEM and EDX analysis.

References

1. Lynch SE, Genco RJ, Marx RE (1999) Tissue engineering: applications in maxillofacial surgery and periodontics. Quintessence Publishing Co, Inc
2. Fabri M, Celotti GC, Ravaglioli A (1995) Biomaterials 16:225
3. Ando J (1958) Bull Chem Soc Japan 31(2):196
4. Eisenberg P (1996) J Biomed Mater Res 32:143
5. Kawachi EY, Bertaran CA, Reis RR, Alves OL (2000) Química Nova 23:618
6. Lorenzo LMR, Regi MV (2000) Chem Mater 12:2460
7. Rhee SH (2002) Biomaterials 23:1147
8. Wakamura M, Kandori K, Ishikawa T (1997) Polyhedron 16:2047
9. Balamurugan K, Vasant C, Rajaram R, Ramasami T (1999) Biochim Biophys Acta 1427:357
10. ATSDR- Agency for toxic substances and disease registry (2000) Toxicological profile for chromium. Syracuse. US Department of Health & Human Services
11. Powel RC (1998) Physics of solid-state laser materials. Springer-Verlag, New York, p 215
12. Grinberg M (2002) Opt Mater 19:37
13. Patra A, Tallman RE, Weintein BA (2005) Opt Mater 27:1396
14. Fromzel VA, Prasad CR (2001) J Phys Chem Solids 62:865
15. Parsons-Karavassilis D, Gu Y, Ansari Z, French PMW, Taylor JR (2000) Optics Commun 181:361
16. Ravikumar RVSSN, Chandrasekhar AV, Rao SN, Madhu N, Reddy BJ, Reddy YP (1999) Cryst Res Technol 34:911
17. Driessens FCM, Boltong MG, de Maeyer EAP, Wenz R, Nies B, Planell JA (2002) Biomaterials 23:4011
18. Miyake M, Watanabe K, Nagayama Y, Nagasawa H, Suzuki T (1990) J Chem Soc Faraday Trans 86:2303
19. Ishikawa K, Ducheyne P, Radin S (1993) J Mater Sci: Mater Med 4:165
20. Moss TS (1973) Semiconductor Opto-electronics, Butterworths, London, p 48, chap. 3
21. Mott NF, Davis EA (1979) Electronic process in non-crystalline materials. Clarendon Press, Oxford
22. Urbach F (1953) Phys Rev 92:1324
23. Calderín L, Stott MJ, Rubio A (2003) Phys Rev B 67:134106
24. Powel RC (1998) Physics of solid-state laser materials. Springer-Verlag, New York, pp 215–253